Deep learning-assisted prediction and profiled membrane microstructure inverse design for reverse electrodialysis

Lu Wang, Yanan Zhao, Liu Zhichun, Wei Liu, Rui Long [*]

School of Energy and Power Engineering, Huazhong University of Science and Technology, Wuhan, 430074, China

ARTICLE INFO

ABSTRACT

Compared to traditional inter-membrane spacers, profiled ion exchange membranes significantly improve the energy harvesting performance of reverse electrodialysis (RED). Here computational fluid dynamics is employed to generate data regarding the flow and mass transfer characteristics and performance index under different profiled membrane microstructures. Data-driven deep learning models are constructed for microstructure shape generation, physics field prediction, and performance forecasting. Results show that the microstructure shape generation via the Bezier generative adversarial network, the physical field prediction via conditional generative adversarial network for the velocity field and the performance prediction via multi-layer perceptron for power number and Sherwood number achieves satisfied accuracy, respectively. The gradient descent algorithm is utilized to optimize the microstructure shape achieving higher mass transfer performance and lower pump power consumption. Compared to the traditional straight ridge channel, the optimized microstructure channel exhibits a reduction of 18.85 % in the power number and an increase of 41.00 % in the Sherwood number, rendering significantly boosted performance.

1. Introduction

With the rapid growth of the global population, the energy demand is exponentially increasing. Regarding resource depletion and escalating climate crises, developing and utilizing renewable energy sources has become a crucial strategy all over the world [1]. Salinity gradient energy (SGE) is a kind of clean energy source originating from the electrochemical potential difference between solutions of different salt concentrations, with no thermal pollution or generation of harmful substances, also known as "blue energy" [2,3]. It is estimated that the energy available worldwide from the convergence of rivers and oceans is about 2.6 TW [4], accounting for approximately 20 % of global energy demand [5]. Additionally, industrial brine and high salinity household wastewater can also provide significant SGE sources [6,7]. Reverse electrodialysis (RED) is one of the most mature technologies for SGE harvesting, which directly converts SGE into electricity without intermediate energy conversion stages and exhibits high energy density and strong resistance to pollution [8]. Furthermore, RED is widely investigated and used in hydrogen production [9,10] and wastewater treatment [11,12].

Factors affecting the RED performance mainly are solution flow rate

[13], temperature [14], multivalent ions [15], stack configuration [16], and membrane properties [17]. In the RED process, the concentration polarization phenomena exists (increased salt concentration at the membrane surface in the dilute channel and decreased salt concentration at the membrane surface in the concentrate channel), which lowers voltage of the RED stack [18]. Flow channels can significantly influence RED performance. The most common channel is formed by the spacer with a net of filaments, which promotes flow mixing and reduces concentration polarization [19]. Traditional spacers are made of non-conductive polymeric materials such as polyamide and polypropylene, which increase the electrical resistance of channels and reduce the contact area between ion exchange membranes and solutions, leading to a "shadow effect" that negatively impacts RED performance [20]. Mehdizadeh et al. [21] investigated the RED stacks using 16 different spacers with varying porosity and geometric shapes, demonstrating that the shadow effect significantly increases stack resistance. Długołęcki et al. [22] developed conductive RED spacers, which increased stack power density by 3–4 times than non-conductive spacers.

To overcome the limitations of traditional spacers, the concept of profiled ion exchange membranes has been proposed in recent years.
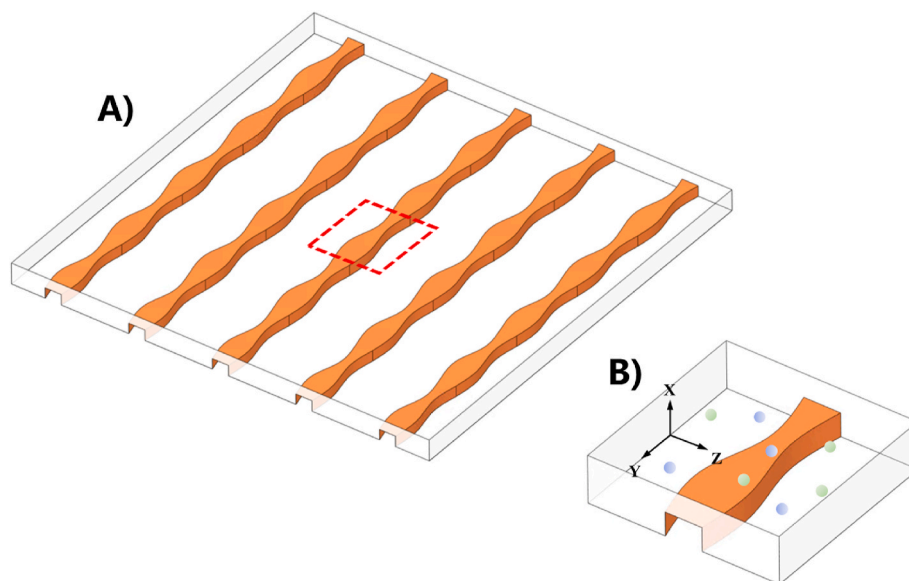

Fig. 1. A) Microstructure channel with the single-sided profiled membrane; B) Unit cell.

The "spacerless membranes", feature customized microstructures such as ridges, waves, relief, and pillars are developed [23]. These microstructures form grooves or protrusions with the membrane material and support the entire flow channel, eliminating the shadow effect caused by spacers and exhibiting excellent conductivity. Compared to traditional spacers, profiled membranes can significantly reduce hydraulic losses and ohmic resistance, effectively improving RED performance with higher economic feasibility and less sensitivity to fouling [24]. Vermaas et al. [25] applied profiled membranes with straight ridges to the RED stack. The profiled membranes exhibited lower permselectivity and ohmic resistance, which significantly reduced hydraulic friction and increased net power density. Güler et al. [26] investigated profiled anion exchange membranes with straight ridges, waves, and pillars, which were assembled on the low concentration side of the RED stack. Pawlowski et al. [27] conducted CFD simulations of flow and mass transfer in different profiled membrane channels, revealing that the channel with integrated chevron structures achieved the largest power density under a compromise between mass transfer enhancement and pressure drop increase. Dong et al. [28] established a three-dimensional multi-physical model for the RED cell pair and found that the wave-profiled membrane can enhance fluid mixing and ion transfer in channels.

The deep learning developed from neural networks was first proposed by Hinton et al., in 2006 [29], which is grounded by the universal approximation theorem [30]. As a popular branch of machine learning, the deep learning method has been widely adopted in performance prediction, optimization, and surrogate model building. Li et al. [31] adopted the deep learning method to investigate adiabatic film cooling effectiveness distribution with variable operating conditions and geometric layouts, and the prediction fields were in good agreement with the CFD results. Kang et al. [32] developed a deep learning model for three-dimensional transient mixed convection in a horizontal channel with a heated bottom surface, revealing that the conditional generative adversarial network yielded high clarity and accuracy in inferring temperature maps. Li et al. [33] proposed an interactive framework for hydrofoil design and optimization based on deep learning, which realized the mapping of hydrofoil design and operating parameters to hydrodynamic performance parameters, and further completed effective optimization design of hydrofoils. Du et al. [34] employed the deep learning model to predict the physical fields and aerodynamic performance of turbine blades, and further optimized the turbine rotor blade profile with the gradient-based method.

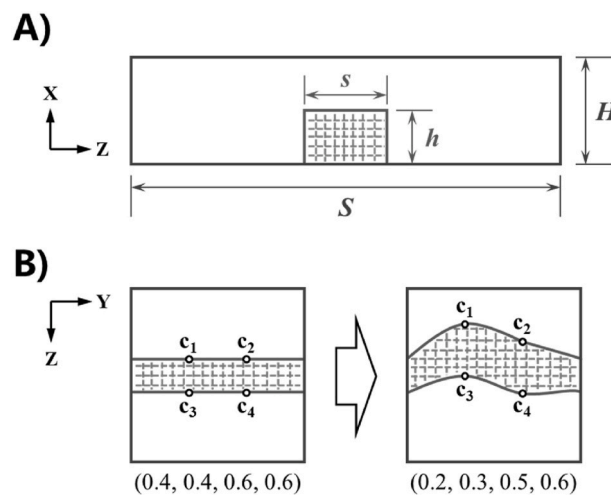Profiled ion exchange membranes overcome the limitations of

Fig. 2. A) Model dimensions; B) Microstructure profile.

traditional spacers and significantly improve the energy conversion generation performance of RED. Designing appropriate microstructures of the profiled ion exchange membranes can significantly upgrade the RED performance. In previous studies, only different basic shapes of microstructures have been investigated. The optimal derived variations of specific microstructures have not been revealed. In this paper, the performance of RED with straight ridge and various derived microstructures is analyzed based on the CFD method. Data-driven deep learning models including microstructure shape generation network, physical field prediction network, and performance prediction network are established. The gradient descent algorithm is further employed to optimize the shape of the profiled membrane microstructure, achieving higher mass transfer performance and lower pump power consumption. The generalization model combining CFD and deep learning facilitates the optimization of RED, and this work may provide guidance for rationally developing and designing high-performance profiled membranes.

2. Materials and methods

2.1. CFD modelling

Here the RED microstructure channel with a single-sided profiled membrane is investigated. The overall structure of the channel is shown in Fig. 1A. The periodic unit of the channel (unit cell) [27,35] is simulated to avoid excessive computational requirements, as depicted in Fig. 1B with the main flow direction coinciding with the z-axis.

Referring to the typical application scope of most industrial membranes, a model aspect ratio is chosen as $S/H = 4$. The specific dimensions of the unit cell are illustrated in Fig. 2A, where the channel height is $H = 260$ μm. A rectangular ridge with a height of $h = 130$ μm is pressed on the membrane to perturb the fluid flow, and the microstructure width is $s = 200$ μm. As shown in Fig. 2B, originating from the straight ridge microstructure, various derived profile shapes of the microstructure are introduced. Four points are selected to generate the microstructure shape curves.

The flow within the periodic unit cell conforms to the three-dimensional steady-state continuity and momentum transport equations [18]:

$$\overrightarrow{\nabla} \cdot \overrightarrow{u} = 0 \tag{1}$$

$$\rho \overrightarrow{u} \overrightarrow{\nabla} \cdot \overrightarrow{u} = -\overrightarrow{\nabla}\widetilde{p} + \mu \nabla^2 \overrightarrow{u} + \overrightarrow{P} \tag{2}$$

where $\overrightarrow{u}$ is the velocity (m·s^{-1}); ρ is the density (kg-m-3); μ is the dynamic viscosity (Pa·s); $\widetilde{p}$ denotes the periodic component of pressure (Pa), with spatial distribution periodically repeating in each unit cell; $\overrightarrow{P}$ is the body force per unit volume (N·m^{-3}), representing the large-scale component of the driving pressure gradient along the main flow direction.

The mass transfer equation can be obtained with the periodic transformation for electrolyte concentration based on the Stefan-Maxwell equation [18]:

$$\overrightarrow{\nabla}(\widetilde{C}\overrightarrow{u}) = \overrightarrow{\nabla}(D\overrightarrow{\nabla}\widetilde{C}) - K_c w \tag{3}$$

where D is the diffusion coefficient of the electrolyte (m^2·s^{-1}); $\widetilde{C}$ is the periodic component of ion concentration (mol·m^{-3}), with spatial distribution periodically repeating in each unit cell; w is the velocity component along the main flow direction (m·s^{-1}); K_c is the large-scale concentration gradient along the main flow direction, i.e., dC/dz (mol·m^{-4}) [18]:

$$K_c = \frac{\overline{J}_{\text{IEM}} \cdot A}{w_{\text{ave}} \cdot V} \tag{4}$$

where A is the surface area of the ion exchange membrane (m^2); V is the volume of the unit cell (m^3); w_{ave} is the volume-averaged velocity along the main flow direction (m·s^{-1}); $\overline{J}_{\text{IEM}}$ is the average flux of electrolyte entering the channel from the walls (mol·m^{-2}·s^{-1}).

The electrolyte flux can be calculated as [18]:

$$\overline{J}_{\text{IEM}} = \pm \frac{0.5j}{F} \tag{5}$$

where j is the current density (A·m^{-2}); F is the Faraday constant (C·mol^{-1}); the electrolyte flux is "+" when ions enter the channel and "−" when ions exit the channel.

The hydraulic diameter of the channel is twice the channel height [18]:

$$d_h = 2H \tag{6}$$

The Reynolds number is calculated as [18]:

Table 1
Physical properties of NaCl aqueous solution [35].

Temperature (°C)	Molarity (M)	Density (kg·m^{-3})	Viscosity (Pa·s)	Diffusivity (m^2·s^{-1})
25	0.5	1017	9.31×10^{-4}	1.472×10^{-9}

$$Re = \frac{\rho w_{\text{ave}} d_h}{\mu} \tag{7}$$

The Fanning friction factor is defined as [18]:

$$f = \frac{\Delta p}{\Delta z} \frac{d_h}{2\rho w_{\text{ave}}^2} \tag{8}$$

where $\Delta p / \Delta z$ is the average pressure gradient along the main flow direction (Pa·m^{-1}).

The pump power consumption is characterized by the dimensionless power number [18]:

$$Pn = \frac{\Delta p}{\Delta z} w_{\text{ave}} \frac{\rho^2 H^4}{\mu^3} = \frac{1}{8} f Re^3 \tag{9}$$

The average mass transfer coefficient for the ion transport process is defined as [18]:

$$k = \frac{\overline{J}_{\text{IEM}}}{\overline{C}_w - C_b} \tag{10}$$

where $\overline{C}_w$ is the average wall concentration (mol·m^{-3}); C_b is the volume-averaged concentration (mol·m^{-3}).

The mass transfer characteristics of the channel are represented by the Sherwood number [18]:

$$Sh = \frac{k d_h}{D} \tag{11}$$

The fluid adopted here is NaCl aqueous solution with a concentration of 0.5 M, representative of typical seawater. The operating temperature of the solution is assumed to be 25 °C, and the corresponding physical properties are listed in Table 1 [35]. Periodic boundary conditions are imposed on the inlet and outlet surfaces perpendicular to the main flow direction, and the surfaces perpendicular to the y-axis are set as translational periodicity boundaries. The profiled membrane and microstructure surfaces are considered non-slip walls, and a negative electrolyte flux is imposed at the non-microstructured portion of the membrane surfaces to simulate ion efflux. Due to the concentration polarization at higher current densities, a high current density of $i = 60$ A m^{-2} is selected to analyze the mass transfer capability of the channel under extreme operating conditions. For different microstructure channels, the average pressure gradient is fixed as $\Delta p/\Delta z = 5000$ Pa m^{-1} to study the effect of variations in microstructure shape on the flow and mass transfer performance of the channel under lower Reynolds numbers ($Re < 4$).

The geometric model is meshed multiple times to obtain eight sets of grids with quantities ranging from approximately 0.15 million to 2.8 million, and the dimensionless power number and Sherwood number are calculated for different grid numbers. Fig. 3 presents the impact of grid numbers on Pn and Sh. As the grid number increases from 2.03×10^6 to 2.80×10^6, the minimum change rates of 0.15 % for the dimensionless power number and 0.26 % for the Sherwood number occur, indicating that further grid refinement has little effect on simulation and the computed results are independent of the grid quantity. Therefore, a grid number of 2.03×10^6 is selected for CFD analysis.

The flow and mass transfer characteristics within the channel experimented by Li et al. [36] are calculated. The channel studied in the experiment is formed by a net spacer made of overlapped wires, with the ratio of spacer wire spacing to channel height as $S/H = 4$. The corresponding unit cell is depicted in Fig. 4, with the main flow direction
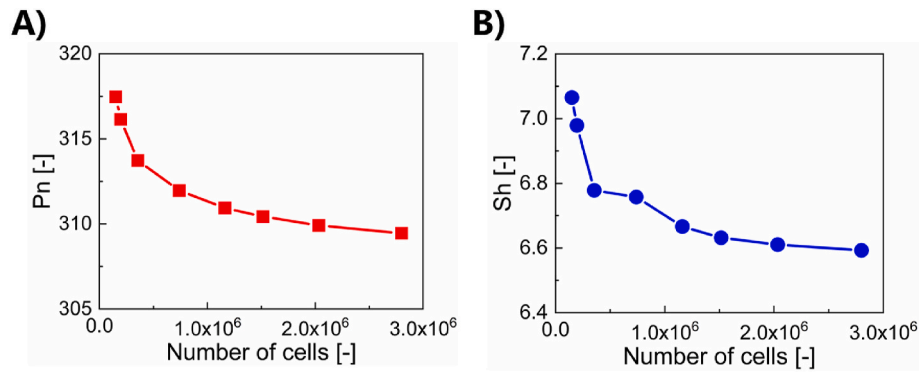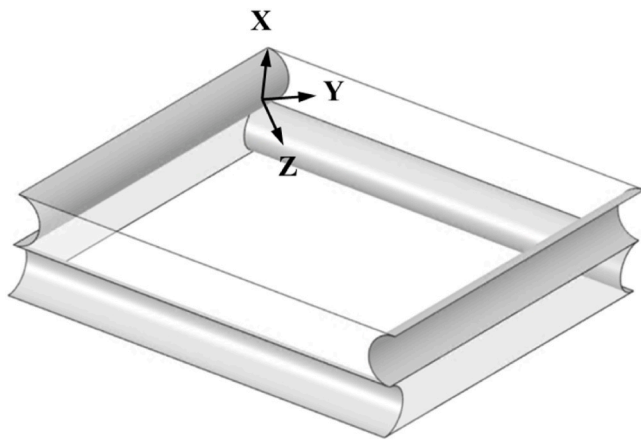
Fig. 3. Grid independence analysis.

Fig. 4. Overlapped spacer unit cell.

Table 2
Physical properties of mixed electrolyte solution [36].

Temperature (°C)	Density (kg·m^{-3})	Viscosity (Pa·s)	Diffusivity (m^2·s^{-1})
20	1034	0.9764×10^{-6}	7.260×10^{-10}

along the z-axis, which bisects the angle formed by the filaments. The working fluid adopted in the experiment is a mixed electrolyte solution, and relevant physical properties are listed in Table 2 [36].

As shown in Fig. 5, the dimensionless power number and Sherwood number obtained from the simulation are compared with experimental results as well as CFD results reported by Li et al. [36] and Gurreri et al. [35], indicating that the variations and values exhibit good consistency with experimental and CFD studies. Therefore, the numerical model employed in this paper can accurately simulate the flow and mass transfer processes.

2.2. Deep learning method

Here, three deep learning networks are constructed: (1) microstructure shape generation network, which utilizes the Bezier generative adversarial network (Bezier-GAN) based on spline shape synthesis [37], enabling direct mapping from geometric parameters to microstructure profile; (2) physical field prediction network, which employs the conditional generative adversarial network (cGAN) based on U-net generator [38], enabling mapping from microstructure profile to concentration and velocity fields; (3) performance prediction network, which adopted the multi-Layer perceptron (MLP) based on fully connected neural layers, enabling mapping from geometric parameters to dimensionless power number and Sherwood number.

2.2.1. Microstructure shape generation network

Bezier-GAN enables dimensionality reduction of curve data, generating control points and further uniform, discrete smooth contour points. The network consists of a generator (G) and a discriminator (D), where the generator receives geometric parameters c and random noise z to generate fake curve samples, and the discriminator receives real samples or fake samples synthesized by the generator, learns to distinguish between these data and predicts the probability that the sample is real. The detailed construction and expressions of the microstructure shape generation network can be seen in the Appendix.

The kernel maximum mean discrepancy (MMD) [39] is used to evaluate the approximation between the generated data distribution and the real data distribution, and assess the quality of synthesized curves:
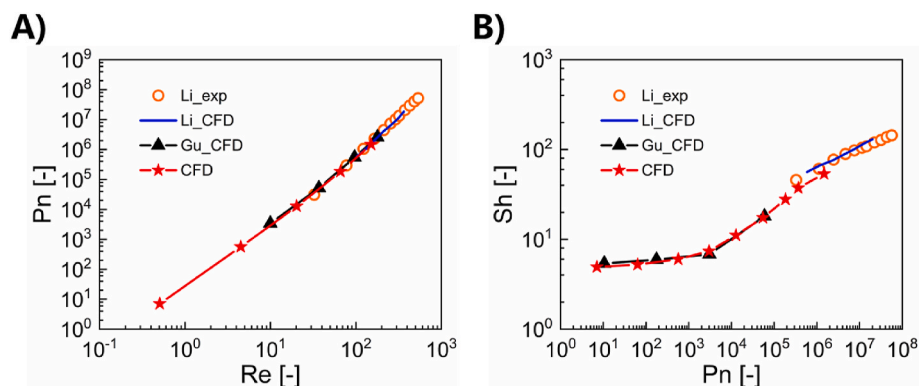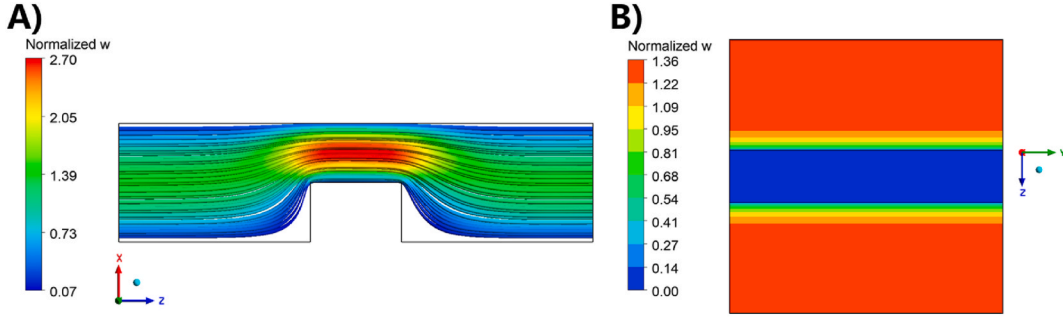

Fig. 5. Model validation.

Fig. 6. A) Streamlines of the straight ridge channel on the x-z midplane; B) Normalized velocity distribution of the straight ridge channel on the y-z midplane.

$$\text{MMD}^2(P_{\text{data}}, P_G) = \mathbb{E}_{x_d,x_d'\sim P_{\text{data}};x_g,x_g'\sim P_G}\left[k(x_d,x_d') - 2k(x_d,x_g) + k(x_g,x_g')\right] \tag{12}$$

where $k(x,x') = \exp(-\|x-x'\|^2/(2\sigma^2))$ is a Gaussian kernel. A lower MMD indicates that the synthesized curves are more realistic.

2.2.2. Physical field prediction network

cGAN incorporates real labels as part of the features, thereby introducing a conditional variable to guide and constrain the generator in synthesizing the desired tensor. The physical field prediction network employs the data-driven mode of cGAN, enabling one-to-one mapping from the microstructure profile to physical fields. The detailed construction and expressions of the physical field prediction network can be seen in the Appendix.

The absolute error between real and predicted data is defined as:

$$\text{Diff} = |X - X'| \tag{13}$$

where X and X' are the real physical field data and the network prediction data, respectively.

The relative root mean square error (RMSE) is used to evaluate the performance of the physical field prediction network [38]:

$$\text{RMSE} = \sqrt{\frac{\sum_{i=1}^{N}(x_i - x_i')^2}{N}} \bigg/ \sqrt{\frac{\sum_{i=1}^{N}x_i^2}{N}}, x_i \in X, x_i' \in X' \tag{14}$$

where x_i and x_i' are the data of the real physical field and the corresponding predicted field, respectively; N is the number of data points. A lower relative RMSE indicates that the predicted data are more realistic.

2.2.3. Performance prediction network

The performance prediction network is based on the architecture of MLP, receiving geometric parameters and predicting the power number and Sherwood number for the corresponding channel. The detailed construction and expressions of the performance prediction network can be seen in the Appendix.

The target relative error (TRE) is defined to evaluate the performance of the performance prediction network:

$$\text{TRE} = \frac{|\psi_m - \psi_m'|}{\psi_m} \tag{15}$$

where ψ_m and ψ_m' represent the real and predicted performance parameters, respectively. A lower TRE indicates more accurate performance prediction.

2.2.4. Data preparation and preprocessing

The data-driven deep learning models require a large amount of high-confidence sample data as input. For the microstructure shape generation network, 660 sets of third-order Bezier curve data are randomly generated. The ratio of the training set to the validation set is

10:1, where each data set contains two contour curves. Four points are uniformly taken along the microstructure shape curves, and corresponding z-axis relative coordinates are combined as the geometric parameters c (c_1,c_2,c_3,c_4). The Latin hypercube sampling method is used to sample geometric parameters within the design space, generating 600 and 60 sets of parameters for training and validation, respectively. To avoid curve interference and exceeding the model boundaries in structural design, the geometric parameters must satisfy certain constraints:

$$\begin{cases} 0 < c_1 < c_3 < 1 \\ 0 < c_2 < c_4 < 1 \end{cases} \tag{16}$$

The geometric parameters are imported into the trained microstructure shape generation network to synthesize microstructure profiles. The profile data are modeled and simulated by the CFD method to obtain the flow and mass transfer characteristics under different channels. The interpolation method is employed to extract the coordinate information, concentration C, and velocity in z-direction w on grid nodes, forming the real physical field with a size of 128×128 for training and validation of the physical field prediction network. The dimensionless power numbers and Sherwood numbers of different channels are calculated to train and validate the performance prediction network.

The data inputs of the deep learning models are all preprocessed by the Min-Max normalization method:

$$\text{data}_i = \frac{\text{data}_i - \min(\text{data})}{\max(\text{data}) - \min(\text{data})} \tag{17}$$

3. Results and discussion

3.1. Performance under the straight ridge channel

Fig. 6A illustrates the streamlines of the straight ridge channel on the x-z midplane parallel to the flow direction, where the normalized velocity in z-direction is represented as w/w_{ave}. The streamlines enter the unit cell from the inlet, converge towards the upper wall due to the perturbation of the straight ridge, and then refill the entire channel after passing through the microstructure. At a lower Reynolds number, there are distinct stagnation regions at the intersection of the lower wall and the base of the straight ridge, with no evident diversion or vortex near the microstructure, and excellent symmetry is observed between the upstream and downstream streamlines. The fluid velocity increases first and then decreases as flow proceeds, attributed to the abrupt reduction in cross-sectional area as the fluid flows through the microstructure, which is more obvious in the domain away from the walls. Fig. 6B shows the velocity distribution of the channel on the y-z midplane parallel to the flow direction. Due to the geometric symmetry of the channel, the velocity contour on the midplane also exhibits excellent symmetry. The fluid velocity decreases first and then increases along the main flow direction, with step changes near the microstructure. The region with optimally developed flow shifts from the midplane towards the upper
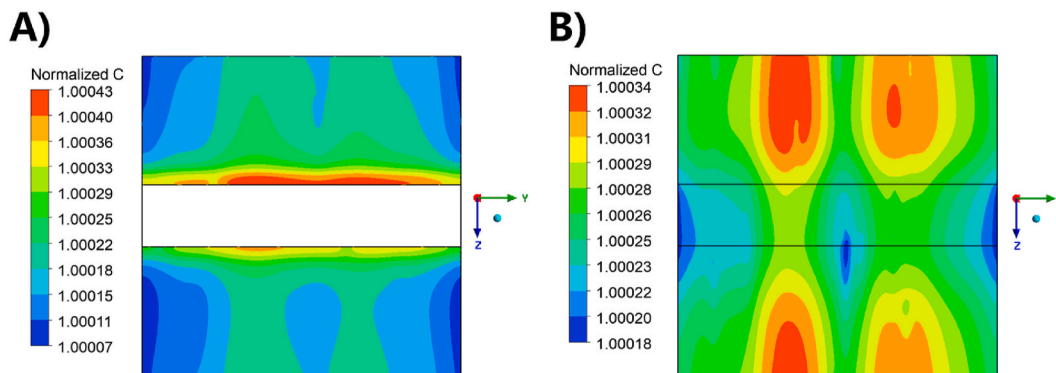
Fig. 7. Normalized concentration distribution of the straight ridge channel: A) The lower wall; B) The upper wall.
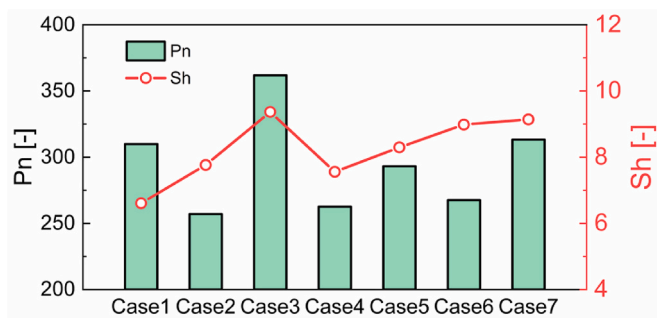

Fig. 8. Performance of different microstructure channels.

wall due to the obstruction of the microstructure, resulting in uniform velocity distribution and a maximal flow velocity away from the microstructure. However, the flow development near the microstructure gradually weakens, and even stagnation occurs on the microstructure surface.

Fig. 7 illustrates the concentration distributions of the straight ridge channel on the lower and upper walls, where the normalized concentration of the wall is defined as C_b/C_w. The symmetry feature of the geometry also applies to the concentration field. For the lower wall, a maximal normalized concentration appears at the intersection of the straight ridge and the lower wall, indicating a strong concentration polarization near this area, while the mass transfer is better away from the straight ridge. Under the disturbance of the microstructure, there is a flow trend in the upstream region away from the lower wall and close to the upper wall, which leads to a gradual increase in the velocity component perpendicular to the main flow direction, and further weakens the mass transfer at the lower wall. Subsequently, the fluid refills the entire unit cell in the downstream region, resulting in a

gradual increase in the velocity component along the main flow direction and enhancing the mass transfer. For the upper wall, the mass transfer near the straight ridge is significantly better than in other areas. The upper wall is flushed by the fluid with a larger velocity component perpendicular to the main flow direction, resulting in a more thorough flow mixing, which is favorable for mass transfer. However, there is less mass transfer in the low-velocity areas near the inlet and outlet.

In the RED process, reducing the hydraulic loss and increasing the output power, are both anticipated, equivalent to achieving a lower dimensionless power number and a higher Sherwood number. Fig. 8 illustrates the performance of the unit cell with different microstructures, where Case 1 represents the straight ridge and Cases 2 to 7 represent six derived microstructures randomly generated. Upgraded performance can be observed under different microstructures. Therefore achieving the optimal microstructure channel is highly demanded.

3.2. Microstructure shape generation

The batch method is adopted for training the microstructure shape generation network, which can improve the training effect and enhance the generalization ability of the generated model, with a batch size of 80. Fig. 9 illustrates the comparison between the microstructure shape curves (discrete red points) generated by Bezier-GAN and the real samples (black lines), which shows that the synthesized curves closely match the real shapes. The kernel MMD of the network according to the validation set is 0.1151 ± 0.0020, indicating that the curves generated using geometric parameters can replace real curves for structural design.

3.3. Physical field prediction

The physical field cGAN is employed to predict the distributions of physical quantities that characterize the flow and mass transfer properties of the channel, including the velocity field on the y-z midplane, as
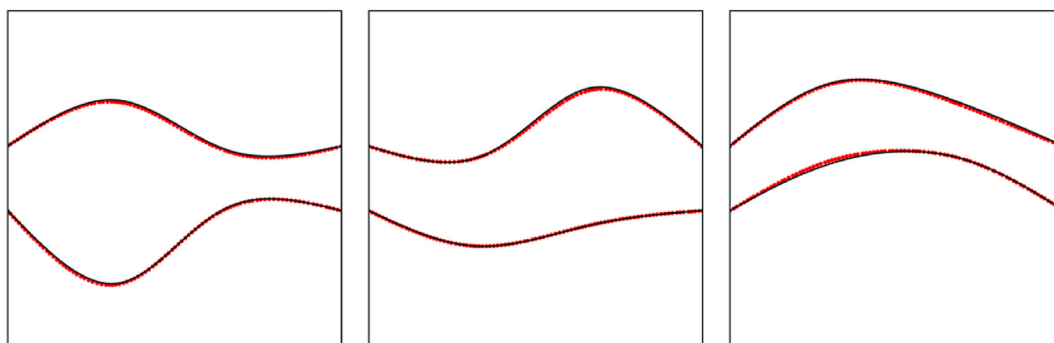

Fig. 9. Accuracy of the microstructure shape generation network. The black lines represent the real samples, and the discrete red points are generated by Bezier-GAN.
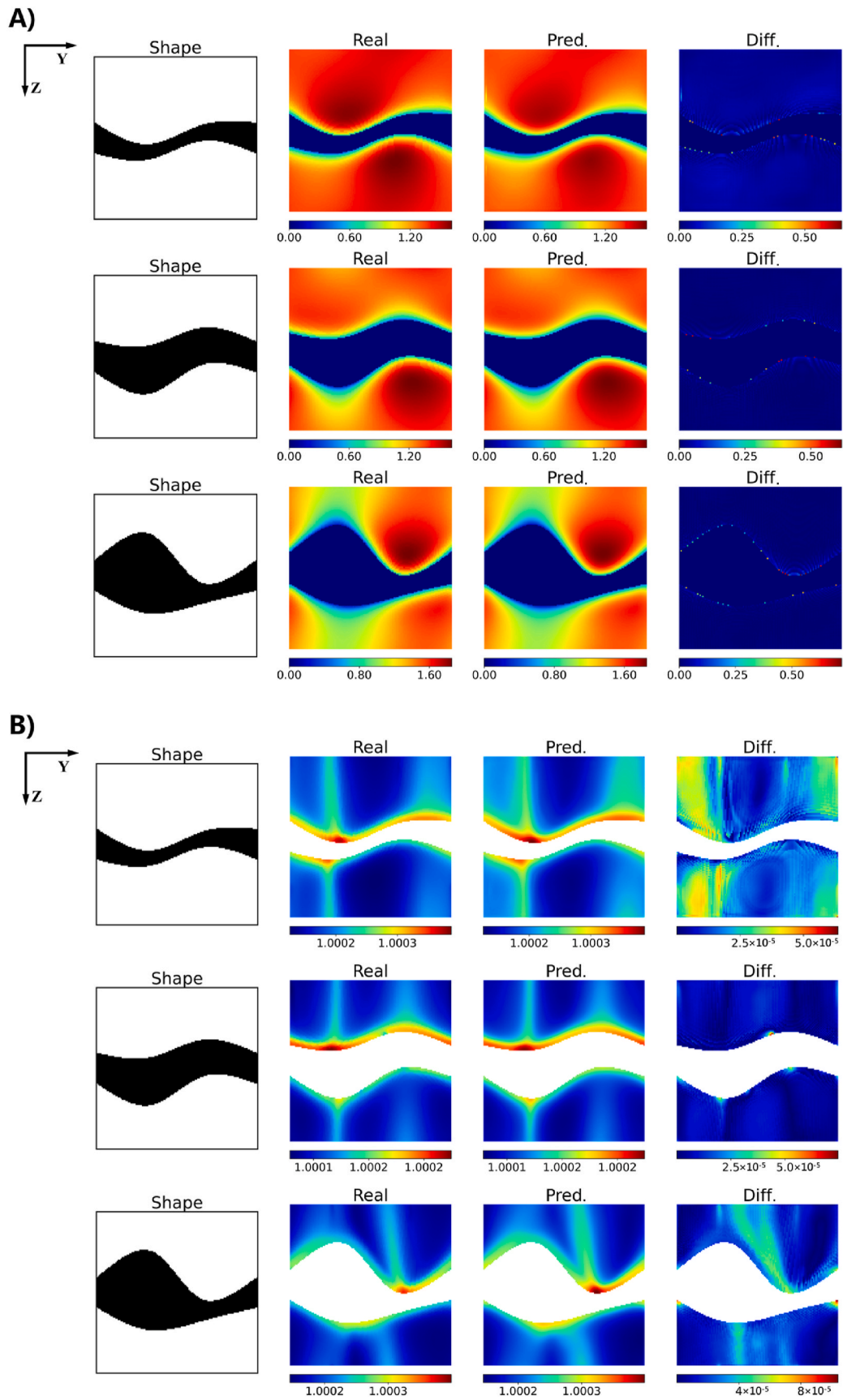
Fig. 10. Accuracy of the physical field prediction networks: A) Normalized velocity field on the y-z midplane; B) Normalized concentration field on the lower wall; C) Normalized concentration field on the upper wall.
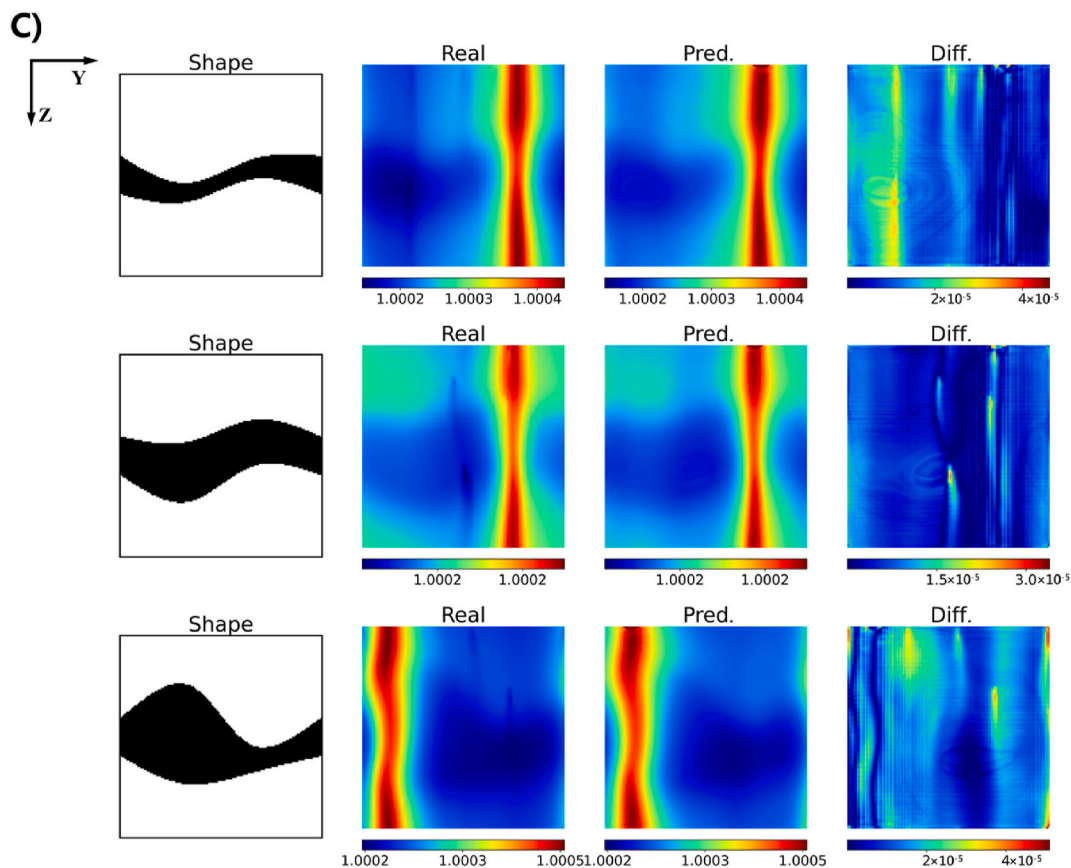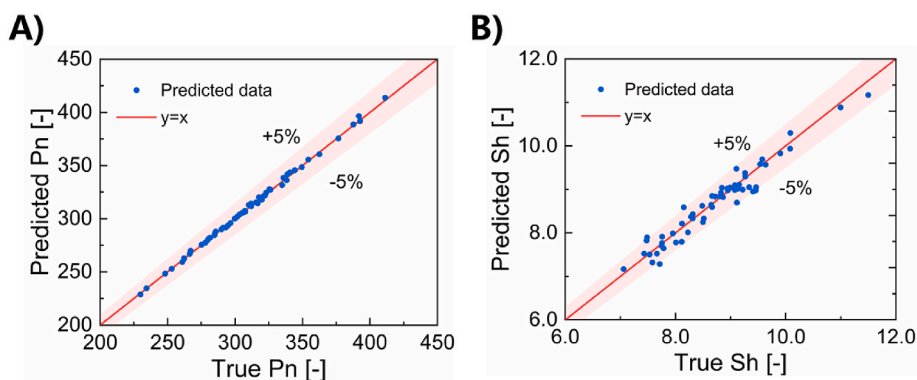
Fig. 10. (*continued*).

Fig. 11. Validation of the performance prediction network.

well as the concentration fields on the lower and upper walls.

For the velocity field on the y-z midplane, the model has the lowest average relative RMSE of 2.104 % at the 3.8×10^5th training step, with a maximum outlier of 4.370 %. For the concentration field on the lower wall, the model has the lowest average relative RMSE of 1.093 % at the 2.4×10^5th training step, with a maximum outlier of 3.447 %. For the concentration field on the upper wall, the model has the lowest average relative RMSE of 0.002 % at the 3.2×10^5th training step, with a maximum outlier of 0.007 %. Fig. 10 presents the comparison between the real and predicted physical fields for different channels, indicating higher prediction accuracy of the models. The relative errors mainly concentrate around the edges of the microstructure, attributing to fewer data points and obvious numerical discontinuity near the microstructure. Therefore, the predicted physical fields can replace real physical fields for flow and mass transfer performance analysis.

3.4. Performance prediction

The batch gradient descent method is employed to update MLP network parameters and weights. Fig. 11 demonstrates the comparison between the predicted and real performance parameters according to the validation set. The average TRE for the dimensionless power number is 0.402 % with a maximum outlier of 1.207 %, and the average TRE for the Sherwood number is 2.257 % with a maximum outlier of 5.591 %. Additionally, the relative errors of most samples are lower than 2.5 %. Overall, the prediction accuracy is satisfying.

3.5. Microstructure optimization

The shape of the microstructure impacts the flow and mass transfer characteristics therefore the energy conversion performance. Under the
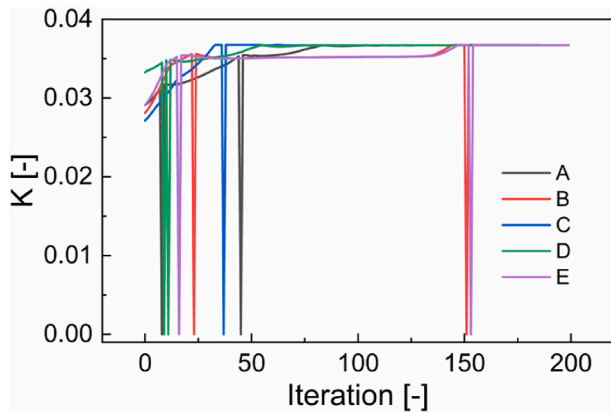
Fig. 12. Optimization search processes with different initial values.

Table 3
Performance of the straight ridge and the optimal microstructure channels.

	Straight ridge channel	Optimal microstructure	Relative change
Pn	309.91	251.50	−18.85 %
Sh	6.61	9.32	+41.00 %
K	0.021	0.037	+76.19 %

automatic differentiation function of the deep learning model [40], the gradient-based method is adopted to optimize the structural parameters. As higher mass transfer performance and lower pump power

consumption are demanded, the ratio of the Sherwood number and the dimensionless power number is employed as the objective function:

$$K = \frac{Sh}{Pn} \tag{18}$$

The differential expression of the objective function with the structural parameters is constructed as:

$$\nabla K = \left[\frac{\partial K}{\partial c_1}, \frac{\partial K}{\partial c_2}, \frac{\partial K}{\partial c_3}, \frac{\partial K}{\partial c_4}\right]^{\mathrm{T}} \tag{19}$$

Here, the geometric parameters (c_1, c_2, c_3, c_4) of the microstructure are design variables, and 3000 optimizations are performed with different random initial values to avoid the problem of local optima. The optimal values of c, Pn, Sh, and K are (0.1389, 0.3443, 0.6278, 0.8733), 251.50, 9.32, and 0.037, respectively. Fig. 12 illustrates the search processes for the largest K with five different initial values. The same results are obtained within 200 iterations. The abrupt changes of K are due to the penalty term imposed on the intermediate variables that do not satisfy the conditions of Eq. (16), ensuring that the optimization is carried out under the constraints within the design space.

The flow and mass transfer characteristics under the straight ridge channel and the optimal microstructure channel are compared in Table 3. The optimal microstructure significantly improves the mass transfer performance and reduces the hydraulic loss. Fig. 13 illustrates the real and predicted physical fields as well as the error distribution of the optimal microstructure channel. The optimized microstructure has a geometric symmetry, rendering an improved flow field and lowered pump power consumption. Relatively uniform concentration distributions are formed on the upper and lower channel walls. The average
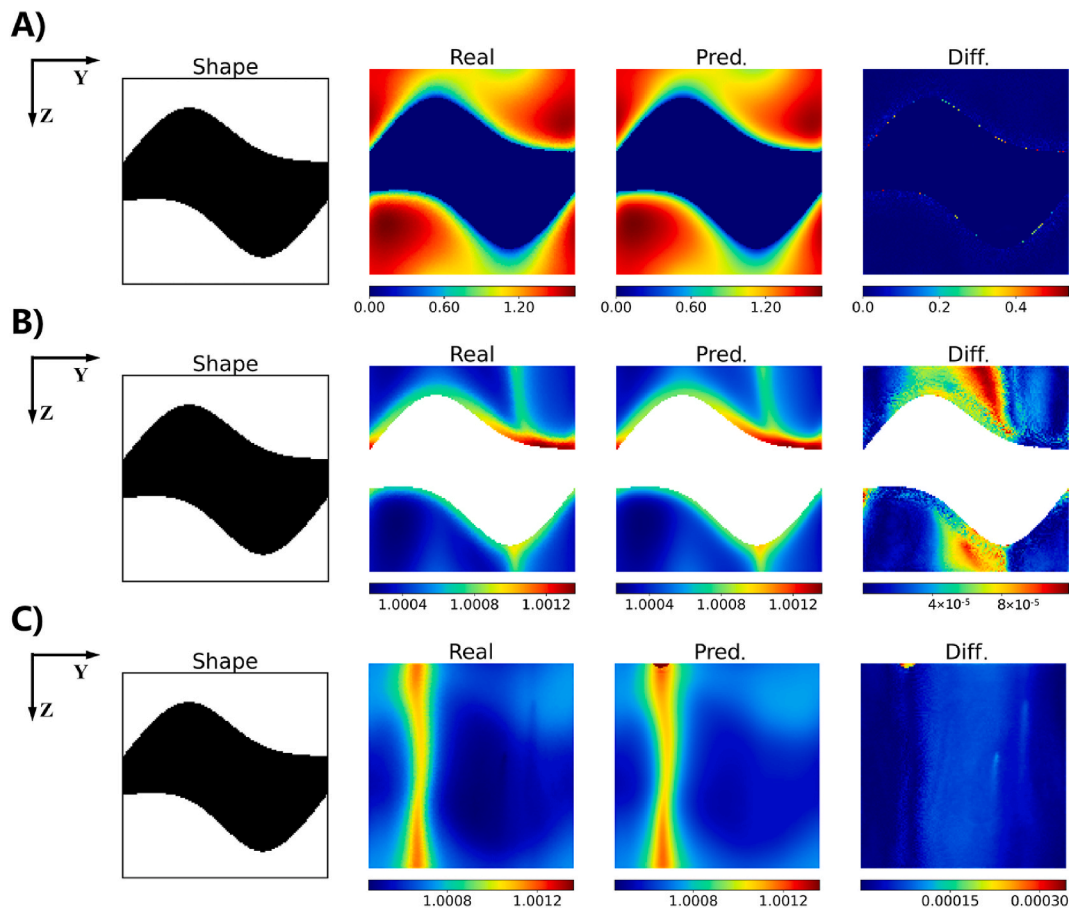

Fig. 13. Prediction field of the optimized microstructure channel: A) Normalized velocity field on the y-z midplane; B) Normalized concentration field on the lower wall; C) Normalized concentration field on the upper wall.

normalized concentration on the walls is lower than that of the straight ridge channel, resulting in upgraded mass transfer performance.

4. Conclusions

In the present study, computational fluid dynamics is employed to generate data regarding the flow and mass transfer characteristics under different profiled membrane microstructures. Data-driven deep learning models are constructed for microstructure shape generation, physics field prediction, and performance forecasting. The main conclusions are.

(1) Under the disturbance of the microstructure, strong concentration polarization occurs at the intersection of the straight ridge and the lower wall, while mass transfer near the straight ridge on the upper wall is observed.

(2) The microstructure shape geometries can be can accurately generated via the Bezier generative adversarial network. The physical field prediction networks successfully predict the velocity field on the y-z midplane and the concentration fields on the lower and upper walls based on the microstructure profile, with average relative RMSEs of 2.104 %, 1.093 %, and 0.002 %, respectively. The performance prediction network presents an average TRE of 0.402 % for the dimensionless power number and 2.257 % for the Sherwood number.

(3) The optimization for the microstructure shape is performed based on the gradient descent algorithm. Compared to the straight ridge channel, the optimized microstructure channel exhibits a reduction of 18.85 % in the power number and an increase of 41.00 % in the Sherwood number.

CRediT authorship contribution statement

Lu Wang: Writing – original draft, Methodology. **Yanan Zhao:** Visualization. **Liu Zhichun:** Formal analysis. **Wei Liu:** Writing – review & editing. **Rui Long:** Writing – review & editing, Supervision, Conceptualization.

Declaration of competing interest

The authors declare that they have no known competing financial interests or personal relationships that could have appeared to influence the work reported in this paper.

Acknowledgments

Appendix

A1 Microstructure shape generation network

The generator of Bezier-GAN contains an input layer, a middle layer, and a Bezier layer. The input layer converts the two-dimensional feature tensor into a three-dimensional tensor or parameter variables through fully connected operations. The middle layer adjusts the tensor size through deconvolution and convolution operations to generate curve control points and corresponding weights. The Bezier layer utilizes control points, weights, and parameter variables to compute curve data into a discrete form as shown in Eq. (A1) [37]. The discriminator consists of a preprocessing layer, a convolutional layer, and an output layer. The preprocessing layer transforms sample data into a three-dimensional tensor. The convolutional layer adjusts the tensor size and extracts the sample information. The output layer maps the feature tensor to an authenticity probability through fully connected operations.

$$x_i = \frac{\sum_{j=0}^{m} \binom{m}{j} t_i^j (1-t_i)^{m-j} P_j w_j}{\sum_{j=0}^{m} \binom{m}{j} t_i^j (1-t_i)^{m-j} w_j}, i = 0, \ldots, n \tag{A1}$$

where x_i represents the data point on the synthesized curve; m is the Bezier degree; P_j is the control point; w_j is the corresponding weight; t_i is the parameter variable satisfying $0 = t_0 < t_{i-1} < t_i < t_n = 1$, which can be obtained by generating the interval variable $\delta_i = t_i - t_{i-1}$ through a softmax activation and then computing the cumulative sum of δ_i.

Backpropagation is adopted to update the model parameters during network training, and the Bernstein polynomial is computed via natural logarithm to enhance the stability of numerical training [37]:

$$B_j^m(t) = \binom{m}{j} t^j (1-t)^{m-j} = \exp(\log \Gamma(m+1) - \log \Gamma(j+1) - \log \Gamma(m-j+1) + j \log t + (m-j)\log(1-t)) \tag{A2}$$

The generator of Bezier-GAN takes geometric parameters as additional inputs and achieves accurate mapping by maximizing the mutual information $I(c; G(c, z))$ between geometric parameters and the generated samples, introducing a regularization constraint as follows [37]:

$$L_I(G, Q) = \mathbb{E}_{x \sim P_G} \left[\mathbb{E}_{c' \sim P(c|x)} [\log Q(c'|x)] \right] + H(c) \tag{A3}$$

where Q is the auxiliary distribution approximating $P(c|x)$; $H(c)$ is the entropy of geometric parameters.

Therefore, the loss function for Bezier-GAN can be expressed as [37]:

$$\min_{G,Q} \max_{D} \mathbb{E}_{x \sim P_{\text{data}}} [\log D(x)] + \mathbb{E}_{c \sim P_c, z \sim P_z} [\log(1 - D(G(c, z)))] - L_I(G, Q) \tag{A4}$$

A2 Physical field prediction network

The generator of the physical field prediction network is based on the U-net model with skip connections and a symmetric network architecture, which is beneficial for achieving good prediction performance on limited data [41]. The generator consists of an input layer, a downsampling layer, an upsampling layer, and an output layer. The input layer maps the microstructure profile tensor to the hidden layer size through a convolution operation. The downsampling layer extracts tensor features through six contracting blocks, and each contracting block performs two convolution operations followed by a max pool operation. The upsampling layer passes tensor features through six expanding blocks, and each expanding block executes upsampling, tensor cropping, skip connection, and three convolution operations. The output layer outputs the physical field tensor through a convolution operation.

The discriminator of the physical field prediction network receives a combined tensor of the microstructure profile and the physical field, outputting a matrix containing discriminative information. The discriminator consists of an input layer, a downsampling layer, and an output layer. The input layer maps the input tensor to the hidden layer size through a convolutional operation. The downsampling layer identifies tensor features through four contracting blocks, and each contracting block performs two convolution operations followed by a max pool operation. The output layer outputs a discriminative matrix through a convolution operation.

In order to prevent the vanishing gradient problem and enhance the training stability of the physical field prediction network, the Wasserstein loss i.e. W loss is adopted [42]. The W loss defines the Earth-Mover (EM) distance to evaluate the approximation between two distributions [38]:

$$\ell_a = \frac{1}{B}\sum_{i=1}^{B} D(I_i, O_i) - \frac{1}{B}\sum_{i=1}^{B} D(I_i, O_i') \tag{A5}$$

where B is the batch size; I represents the microstructure profile; O represents the physical field; $D(I_i, O_i)$ and $D(I_i, O_i')$ are the output matrixes from the discriminator for recognizing real and fake samples, respectively.

For training the generator, the L1 norm is introduced to improve model prediction performance [43]:

$$\ell_r = \frac{1}{B}\sum_{i=1}^{B} |O_i' - O_i| \tag{A6}$$

The Lipschitz continuity of the weights matrix in the discriminator is crucial for training convergence [42]. The gradient penalty method introduces a regularization term into the loss function and imposes a weight restriction when the discriminator gradient norm exceeds one, enforcing the discriminator to be Lipschitz continuous. The gradient penalty term for the physical field prediction network is calculated as follows [38]:

$$\wp_p = \frac{1}{B}\sum_{i=1}^{B} (\|\nabla D(I_i, O_i'')\|_2 - 1)^2 \tag{A7}$$

where O_i'' is a combination of real and synthesized samples [38]:

$$O_i'' = \varepsilon_i O_i + (1 - \varepsilon_i)O_i' \tag{A8}$$

where ε_i is a random number from a uniform distribution on the interval of [0,1].

Therefore, the loss function for the physical field prediction network can be expressed as [38]:

$$\min_{G}\max_{D}\left[\ell_a + \lambda_r \ell_r + \lambda_p \wp_p\right] \tag{A9}$$

where λ_r is a coefficient of the L1 norm; λ_p is a coefficient of the gradient penalty regularization.

The adaptive moment estimation (ADAM) algorithm [44] is used to train the network, and the learning rate is adjusted by the cosine anneal method:

$$\eta_c = \eta_{\min} + \frac{1}{2}(\eta_{\max} - \eta_{\min})\left(1 + \cos\left(\frac{\text{step}_c}{\text{step}_f}\pi\right)\right) \tag{A10}$$

where step_c and step_f are the current step and the final step, respectively; η_c is the learning rate at the current step; $\eta_{\max}$ is the initial learning rate; $\eta_{\min}$ is the termination learning rate.

A3 Performance prediction network

The performance prediction network consists of an input layer, a hidden layer, and an output layer. The input layer gets the training data, the hidden layer extracts tensor features through fully connected operations, and the output layer outputs the target parameters through a fully connected operation. The back-propagation is performed in network training to update neuron weights, minimizing the error between predicted data and real data. To prevent overfitting behavior and improve the generalization capability of the model, the mean square error is used as the loss function:

$$\min \frac{1}{n}\sum_{i=1}^{n}(y_i - y_i')^2 \tag{A11}$$

where y_i and y_i' represent the real and predicted data, respectively.

The exponential decay method is employed to adjust the learning rate:

$$\eta_c = \eta_{\max} r_d^{\left(\frac{\text{step}_c}{\text{step}_d}\right)} \tag{A12}$$

where r_d is the decay rate; step_d is the decay speed.

A4 The training of physical field prediction networks

The mini-batch method is adopted in training physical field prediction networks, and Fig.A1 illustrates the training losses of the generator and discriminator for each network. Backpropagation is performed to update the parameters of the generator and discriminator one time per step, and the physical field prediction networks converge well.
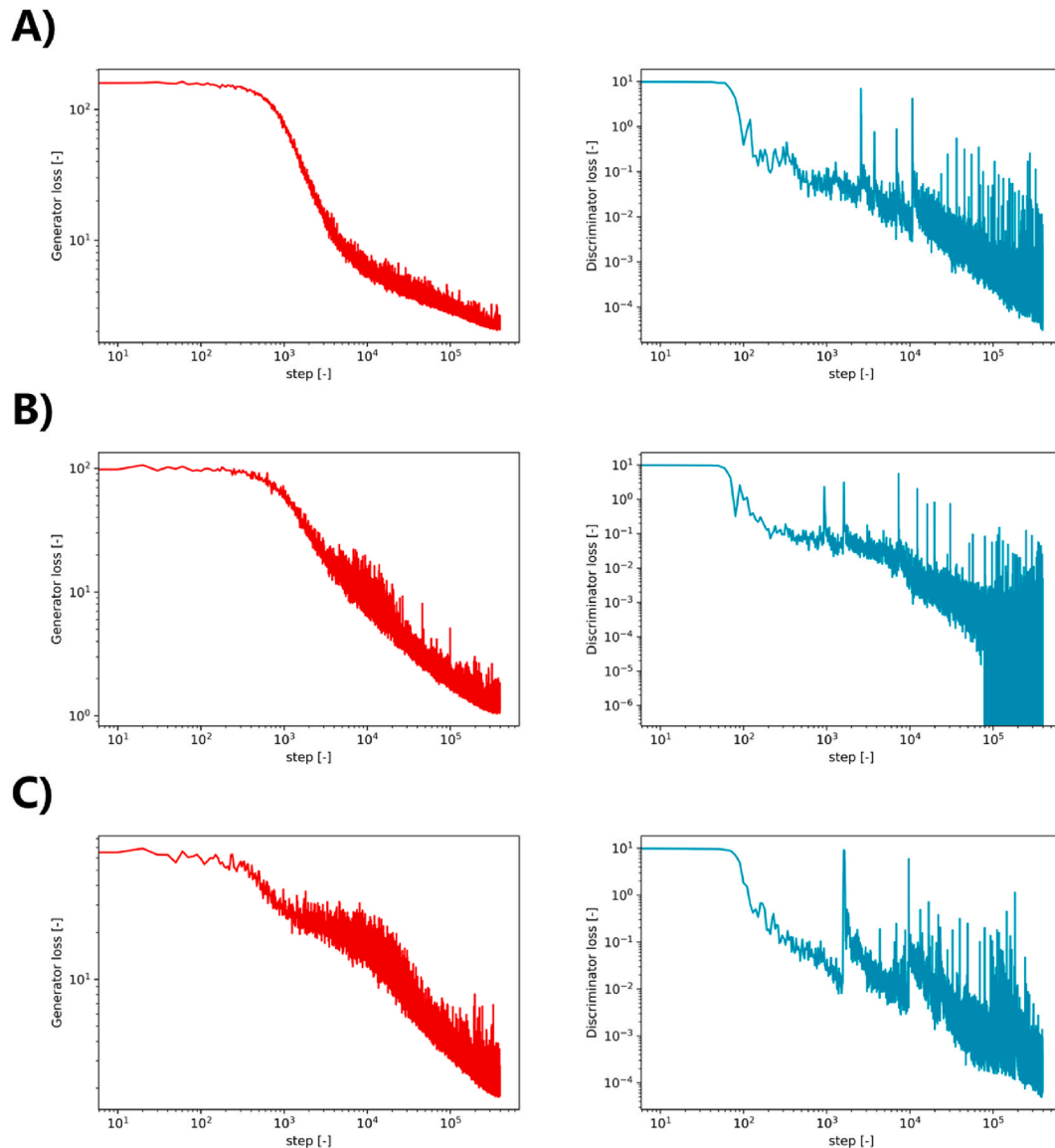

Fig. A1. Training losses for the physical field prediction networks: A) Normalized velocity field on the y-z midplane; B) Normalized concentration field on the lower wall; C) Normalized concentration field on the upper wall.

Data availability

Data will be made available on request.

References

[1] Garratt A, Petrella I, Zhang Y. Asymmetry and interdependence when evaluating U. S. Energy Information Administration forecasts. Energy Econ 2023;121:106620.

[2] Ortiz-Imedio R, Gomez-Coma L, Fallanza M, Ortiz A, Ibañez R, Ortiz I. Comparative performance of salinity gradient power-reverse electrodialysis under different operating conditions. Desalination 2019;457:8–21.

[3] Long R, Luo Z, Kuang Z, Liu Z, Liu W. Effects of heat transfer and the membrane thermal conductivity on the thermally nanofluidic salinity gradient energy conversion. Nano Energy 2019:104284.

[4] Weinstein JN, Leitz FB. Electric power from differences in salinity: the dialytic battery 1976;191(4227):557–9.

[5] Post JW, Veerman J, Hamelers HVM, Euverink GJW, Metz SJ, Nymeijer K, et al. Salinity-gradient power: evaluation of pressure-retarded osmosis and reverse electrodialysis. J Membr Sci 2007;288(1):218–30.

[6] Tufa RA, Pawlowski S, Veerman J, Bouzek K, Fontananova E, di Profio G, et al. Progress and prospects in reverse electrodialysis for salinity gradient energy conversion and storage. Appl Energy 2018;225:290–331.

[7] Daniilidis A, Vermaas DA, Herber R, Nijmeijer K. Experimentally obtainable energy from mixing river water, seawater or brines with reverse electrodialysis. Renew Energy 2014;64:123–31.

[8] Mejía-Marchena R, Maturana-Córdoba A, Fernández-Rojano S. Unveiling the enhancing potential of water pretreatment on energy efficiency in reverse electrodialysis systems - a comprehensive review. J Water Proc Eng 2023;56: 104548.

[9] Wu X, Chen Z, Han Z, Wei Y, Xu S, Zhu X. Hydrogen and electricity cogeneration driven by the salinity gradient from actual brine and river water using reverse electrodialysis. Appl Energy 2024;367:123320.

[10] Wu X, Zhang Y, Zhu X, Wei Y, Sun D, Xu S. Experimental performance of a low−grade heat driven hydrogen production system by coupling the reverse electrodialysis and air gap diffusion distillation methods. Energy Convers Manag 2024;301:117994.

[11] Wang S, Wu X, Xu S, Zhang Y. Theoretical research on a multi-stage reverse electrodialysis reactor wastewater treatment system with independent control strategy. Energy Convers Manag 2024;313:118603.

[12] Wang S, Wu X, Xu S, Leng Q, Lv Y. Overall evaluation of a multi-stage reverse electrodialysis reactor series system for organic wastewater treatment and power generation. Energy Convers Manag 2023;292:117413.

[13] Mei Y, Tang CY. Recent developments and future perspectives of reverse electrodialysis technology: a review. Desalination 2018;425:156–74.

[14] Tedesco M, Brauns E, Cipollina A, Micale G, Modica P, Russo G, et al. Reverse electrodialysis with saline waters and concentrated brines: a laboratory investigation towards technology scale-up. J Membr Sci 2015;492:9–20.

[15] Avci AH, Sarkar P, Tufa RA, Messana D, Argurio P, Fontananova E, et al. Effect of $Mg2+$ ions on energy generation by Reverse Electrodialysis. J Membr Sci 2016; 520:499–506.

[16] Long R, Li B, Liu Z, Liu W. Performance analysis of reverse electrodialysis stacks: channel geometry and flow rate optimization. Energy 2018;158:427–36.

[17] Hong JG, Park T-W, Dhadake Y. Property evaluation of custom-made ion exchange membranes for electrochemical performance in reverse electrodialysis application. J Electroanal Chem 2019;850:113437.

[18] Gurreri L, Tamburini A, Cipollina A, Micale G, Ciofalo M. CFD prediction of concentration polarization phenomena in spacer-filled channels for reverse electrodialysis. J Membr Sci 2014;468:133–48.

[19] Nazif A, Karkhanechi H, Saljoughi E, Mousavi SM, Matsuyama H. Recent progress in membrane development, affecting parameters, and applications of reverse electrodialysis: a review. J Water Proc Eng 2022;47:102706.

[20] Długołęcki P, Gambier A, Nijmeijer K, Wessling M. Practical potential of reverse electrodialysis as process for sustainable energy generation. Environ Sci Technol 2009;43(17):6888–94.

[21] Mehdizadeh S, Yasukawa M, Abo T, Kakihana Y, Higa M. Effect of spacer geometry on membrane and solution compartment resistances in reverse electrodialysis. J Membr Sci 2019;572:271–80.

[22] Długołęcki P, Dąbrowska J, Nijmeijer K, Wessling M. Ion conductive spacers for increased power generation in reverse electrodialysis. J Membr Sci 2010;347(1): 101–7.

[23] Liu J, Geise GM, Luo X, Hou H, Zhang F, Feng Y, et al. Patterned ion exchange membranes for improved power production in microbial reverse-electrodialysis cells. J Power Sources 2014;271:437–43.

[24] Chae S, Kim H, Gi Hong J, Jang J, Higa M, Pishnamazi M, et al. Clean power generation from salinity gradient using reverse electrodialysis technologies: recent advances, bottlenecks, and future direction. Chem Eng J 2023;452:139482.

[25] Vermaas DA, Saakes M, Nijmeijer K. Power generation using profiled membranes in reverse electrodialysis. J Membr Sci 2011;385–386:234–42.

[26] Güler E, Elizen R, Saakes M, Nijmeijer K. Micro-structured membranes for electricity generation by reverse electrodialysis. J Membr Sci 2014;458:136–48.

[27] Pawlowski S, Geraldes V, Crespo JG, Velizarov S. Computational fluid dynamics (CFD) assisted analysis of profiled membranes performance in reverse electrodialysis. J Membr Sci 2016;502:179–90.

[28] Dong F, Jin D, Xu S, Wu X, Wang P, Wu D, et al. Three-dimensional multi-physical simulation of a reverse electrodialysis stack with profiled membranes. Desalination 2022;537:115894.

[29] Hinton GE, Salakhutdinov RR. Reducing the dimensionality of data with neural networks. Science 2006;313(5786):504–7.

[30] Cybenko G. Approximation by superpositions of a sigmoidal function. Math Control, Signals, Syst 1989;2(4):303–14.

[31] Li Z, Su L, Wen F, Zeng J, Wang S, Zhang J. Deep learning method for fast prediction of film cooling performance. Phys Fluids 2022;34(4):047111.

[32] Kang M, Phuong Nguyen N, Kwon B. Deep learning model for rapid temperature map prediction in transient convection process using conditional generative adversarial networks. Therm Sci Eng Prog 2024;49:102477.

[33] Li C, Liu B, Wang S, Yuan P, Lang X, Tan J, et al. Tidal turbine hydrofoil design and optimization based on deep learning. Renew Energy 2024:120460.

[34] Du Q, Li Y, Yang L, Liu T, Zhang D, Xie Y. Performance prediction and design optimization of turbine blade profile with deep learning method. Energy 2022;254: 124351.

[35] Gurreri L, Tamburini A, Cipollina A, Micale G, Ciofalo M. Flow and mass transfer in spacer-filled channels for reverse electrodialysis: a CFD parametrical study. J Membr Sci 2016;497:300–17.

[36] Li F, Meindersma W, de Haan AB, Reith T. Experimental validation of CFD mass transfer simulations in flat channels with non-woven net spacers. J Membr Sci 2004;232(1):19–30.

[37] Chen W, Chiu K, Fuge MD. Airfoil design parameterization and optimization using bézier generative adversarial networks. AIAA J 2020;58(11):4723–35.

[38] Kadeethum T, O'Malley D, Fuhg JN, Choi Y, Lee J, Viswanathan HS, et al. A framework for data-driven solution and parameter estimation of PDEs using conditional generative adversarial networks. Nature Computational Science 2021;1 (12):819–29.

[39] Gretton A, Borgwardt KM, Rasch MJ, Schölkopf B, Smola A. A kernel two-sample test. 13(null %J J. Mach. Learn. Res.) 2012:723–73.

[40] Renganathan SA, Maulik R, Ahuja J. Enhanced data efficiency using deep neural networks and Gaussian processes for aerodynamic design optimization. Aero Sci Technol 2021;111:106522.

[41] Ronneberger O, Fischer P, Brox T. U-net: convolutional networks for biomedical image segmentation In: Navab N, Hornegger J, Wells WM, Frangi AF editors. Conference U-net: convolutional networks for biomedical image segmentation, Cham. Springer International Publishing, p. 234-241. .

[42] Arjovsky M, Chintala S, Bottou L. Wasserstein generative adversarial networks. Proceedings of the 34th International Conference on machine learning - volume 70. Sydney, NSW, Australia: JMLR.org; 2017. p. 214–23.

[43] Pandey A, Wang D. On adversarial training and loss functions for speech enhancement. Conference on adversarial training and loss functions for Speech enhancement. p. 5414-5418..

[44] Kingma DP, Ba JJC. Adam: A Method for Stochastic Optimization 2014. abs/ 1412.6980.